8

Exotic States of High Density Matter Driven by Intense XUV/X-Ray Free Electron Lasers

Frank B. Rosmej
Sorbonne Universités, Pierre et Marie Curie, Paris,
Ecole Polytechnique, Laboratoire pour l'Utilisation des Lasers Intenses LULI,
Physique Atomique dans les Plasmas Denses PAPD, Palaiseau
France

1. Introduction

XUV and X-ray Free Electron Lasers (XFEL's) have provided the high energy density physics community with outstanding tools to investigate and to create matter under extreme conditions never achieved in laboratories so far. The key parameters of existing and planed XFEL installations [LCLS 2011, XFEL 2011, SACLA XFEL 2011] are micro focusing (to achieve intensities in access to 10^{16} W/cm^2), short pulse lengths (10-100 fs), tunable photon energy (1-20 keV), small bandwidth and high repetition frequency (some 10 Hz, allowing to accumulate thousands of shots to improve signal to noise ratios).

This makes XFEL installations distinct different from well known synchrotron radiation facilities. The brilliance of XFEL's is more than 10-orders of magnitude higher than modern synchrotrons and this allows for the first time to photo ionize inner-shells of almost every atom in a solid crystal in a single pulse. As the pulse duration is of the order of the Auger time scale an exotic state of matter, a "Hollow Crystal" can be created. The decay of crystalline order can be initiated by a burst of Auger electrons with energies in the X-ray range that heat up the hollow crystal [Galtier et al. 2011]. This is distinct different to synchrotrons: Auger electron production is rare compared to the total number of atoms and Auger electrons do not allow to change the physical properties of the crystal.

Next, the tunable photon energy (with small bandwidth) will permit for the first time to pump selected atomic transitions in the X-ray range. Compared to the well known pumping of low energy transitions by optical lasers, X-ray pumping will allow outstanding steps forward: investigations of dense matter via pumped X-ray transitions that can escape without essential absorption. As it has been the case for LIF (Laser-induced fluorescence) with standard optical lasers, a revolutionary impact is expected via the photo pumping of X-ray transitions. In this respect we discuss novel quantum mechanical interference effects that are predicted to be observable via the characteristic X-ray spontaneous emission of hole states in dense matter.

As synchrotrons might neither allow selective nor efficient pumping (drastic change of atomic populations) XFEL facilities will open a new world for scientific activity.

2. Atomic kinetics driven by intense short pulse radiation fields

Radiation field quantum mechanics in second quantization is the most general approach to study the interaction of radiation fields with atoms. On a unique footing it allows describing atomic population and coherences and provides all necessary matrix elements to take into account elementary atomic processes (cross sections) that influence on the atomic populations and interference effects.

Under the assumption of broadband illumination and/or large collisional broadening the non-diagonal density matrix elements are negligible compared to the diagonal ones (atomic populations) and the so-called atomic population kinetic approach becomes valid [Loudon 2000]. In its most general form, the atomic population kinetics theory describes the transient evolution of any atomic population (e.g., ground states, excited states, multiple excited states, hollow ion states,..) under the influence of any collisional-radiative process. This theory will be outlined below, paying particular attention to external intense sort pulse radiation fields to describe the XFEL interaction with matter.

2.1 Non-equilibrium atomic population kinetics in collisional-radiative regimes

In dense non-equilibrium plasmas, collisions, radiative processes and time dependent evolution are equally important and have therefore to be treated on the same general footing. It is also necessary to include all ionization stages, ground states and excited states (single, multiple, hollow ion states) via the elementary collisional-radiative processes combined with the time dependent evolution operator. We note that time scales of typical free electron laser radiation are of the order of some 10 fs and those of hollow ion transitions scale down to 1-fs. Therefore, simulations of the radiative properties have to include photon relaxation effects together with collisional-radiative population kinetics and radiation field physics and any approximations for the time dependent evolution operator are highly questionable. We therefore consider the exact time evolution of the atomic populations which is given by the following set of differential equations:

$$\frac{dn_{j_Z}}{dt} = -n_{j_Z} \sum_{Z'=0}^{Z_n} \sum_{i_{Z'}=1}^{N_{Z'}} W_{j_Z i_{Z'}} + \sum_{Z'=0}^{Z_n} \sum_{k_{Z'}=1}^{N_{Z'}} n_{k_{Z'}} W_{k_{Z'} j_Z} \tag{2.1.1}$$

n_{j_Z} is the atomic population of level j in charge state Z, Z_n is the nuclear charge, N_Z is the maximum number of atomic levels in charge state Z and $W_{j_Z i_{Z'}}$ is the population matrix that contains the rates of all elementary processes from level j of charge state Z to level i of charge state Z'.

In general, eq. (2.1.1) is a system on non-linear differential equations because the population matrix might contain the populations by itself. Only for special cases the populations matrix W does not depend on the atomic populations and equations (2.1.1) become linear. Equations (2.1.1) provide N differential equations where N is given by:

$$N = \sum_{Z=0}^{Z_n} N_Z \tag{2.1.2}$$

Looking more carefully to the symmetry relations of eq. (2.1.1) one finds that the system contains only (N-1) independent equations for the N atomic populations. We are therefore seeking for a supplementary equation. If we consider atomic populations in the framework of probabilities (like in quantum mechanics) the probability to find the atom in any state is equal to 1:

$$\sum_{Z=0}^{Z_n} \sum_{j_Z=1}^{N_Z} n_{j_Z} = 1 \tag{2.1.3}$$

Eq. (2.1.3) is the desired Nth equation and is called the "boundary condition". The distribution of atomic populations over the various charge stages is readily obtained from the solution of eqs. (2.1.1):

$$n_Z = \sum_{j_Z=1}^{N_Z} n_{j_Z} \tag{2.1.4}$$

n_Z is the population of the charge stage Z. The population matrix is given by

$$W_{ij} = W_{ij}^{col} + W_{ij}^{rad} + W_{ij}^{FEL} \tag{2.1.5}$$

The collisional processes are described by

$$W_{ij}^{col} = n_e C_{ij} + n_e I_{ij} + n_e^2 T_{ij} + n_e R_{ij} + n_e D_{ij} + Cx_{ij} + n_{HP} C_{ij}^{HP} + n_{HP} I_{ij}^{HP} ..... \tag{2.1.6}$$

and the matrix describing the radiative and autoionizing processes is given by

$$W_{ij}^{rad} = A_{ij} + \Gamma_{ij} + P_{ij}^{abs} + P_{ij}^{em} + P_{ij}^{rr} + P_{ij}^{iz} \tag{2.1.7}$$

A_{ij}: Spontaneous radiative decay rate, Γ_{ij}: Autoionization rate, P_{ij}^{abs}: Stimulated photo absorption, P_{ij}^{em}: Stimulated photoemission, P_{ij}^{rr}: Stimulated radiative emission, P_{ij}^{iz}: Photo ionization, C_{ij}: Electron collisional excitation/de-excitation, I_{ij}: Electron collisional ionization, T_{ij}: 3-body recombination (electrons), R_{ij}: Radiative recombination, D_{ij}: Dielectronic capture, Cx_{ij}: Charge exchange, C_{ij}^{HP}: Excitation/de-excitation by heavy particle collisions, I_{ij}^{HP}: Ionization by heavy particle collisions. The radiation field matrix elements W^{FEL} for the external laser radiation (e.g., the XFEL radiation) are given by

$$W_{ij}^{FEL} = W_{ij}^{FEL,PI} + W_{ij}^{FEL,SR} + W_{ij}^{FEL,SA} + W_{ij}^{FEL,SE} \tag{2.1.8}$$

$$W_{ij}^{FEL,PI} = \int_{\hbar\omega_{ij}}^{\infty} d(\hbar\omega)\, \sigma_{ij}^{PI}(\hbar\omega)\, c\tilde{N}(\hbar\omega) \tag{2.1.9}$$

$$W_{ji}^{FEL,SR} = n_e \frac{\pi^2 c \hbar^3}{\sqrt{2}\, m_e^{3/2}} \frac{g_i}{g_j} \int_0^{\infty} dE\, \frac{F(E)}{\sqrt{E}} \sigma_{ij}^{PI}\left(\hbar\omega_{ij} + E\right)\, \tilde{N}\left(\hbar\omega_{ij} + E\right) \tag{2.1.10}$$

$$W_{ij}^{FEL,SA} = \pi^2 c^3 \hbar^3 A_{ji} \frac{g_j}{g_i} \int_0^\infty d(\hbar\omega) \frac{\phi_{ij}(\omega)}{\hbar} \frac{\tilde{N}(\hbar\omega)}{(\hbar\omega)^2} \tag{2.1.11}$$

$$W_{ji}^{FEL,SE} = \pi^2 c^3 \hbar^3 A_{ji} \int_0^\infty d(\hbar\omega) \frac{\phi_{ji}(\omega)}{\hbar} \frac{\tilde{N}(\hbar\omega)}{(\hbar\omega)^2} \tag{2.1.12}$$

$W^{FEL,PI}$ describes photo ionization, $W^{FEL,SR}$ stimulated radiative recombination, $W^{FEL,SA}$ stimulated photo-absorption, $W^{FEL,SE}$ stimulated photo-emission. σ^{PI} is the photo ionization cross section, F(E) the energy distribution function of the continuum electrons, A the Einstein coefficient of spontaneous emission, φ the line profile, c the velocity of light, $\hbar$ is the Planck constant, g the statistical weight of a bound state, ω the angular frequency of the external radiation field, ω_{ij} the atomic transition frequency and $\tilde{N}$ is the number of external photons (those of the Free Electron Laser) per unit volume and energy.

The population matrix elements are not independent from each other. They are connected by first principles of quantum mechanics: the CPT-invariance of the Hamiltonian. This invariance results in the principle of micro-reversibility: to each elementary process there must exist an inverse process. In thermodynamics, this principle is known as "detailed balance". It states that each elementary process is balanced by its inverse. The difference to the principle of micro-reversibility is that the general effect of a process is considered rather than the detailed cross sections by itself. A general set of atomic population equations for non-Maxwellian plasmas need to be based on the principle of micro-reversibility; the interesting reader is refereed to the article of [Rosmej and Lisitsa 2011].

In optically thin plasmas, the spectral intensity distribution of an atomic transition j→ i with frequency ω_{ji} is given by:

$$I_{j_Z i_Z}(\omega) = \frac{\hbar\omega_{j_Z i_Z}}{4\pi} n_{j_Z} A_{j_Z i_Z} \varphi_{j_Z i_Z}\left(\omega, \omega_{j_Z i_Z}\right) \tag{2.1.13}$$

n_{j_Z} is the population of the upper level j, $A_{j_Z i_Z}$ is the spontaneous transition probability for the transition j→ i and $\varphi_{j_Z i_Z}\left(\omega, \omega_{j_Z i_Z}\right)$ is the associated local emission line profile. Eq. (2.1.13) indicates a strong interplay between the atomic structure (means transition probabilities $A_{j_Z i_Z}$) and atomic populations kinetics (population densities n_{j_Z}). The total spectral distribution is given by

$$I(\omega) = \sum_{Z=0}^{Z_n} \sum_{j_Z=1}^{N_Z} \sum_{i_Z=1}^{N_Z} I_{j_Z i_Z}(\omega) \tag{2.1.14}$$

Eq. (2.1.14) is of outstanding importance: it is the spectral distribution that is accessible via measurements (spectroscopy).

In plasmas where opacity in line transitions is important the spectral distribution according eq. (2.1.14) can be modified employing the escape probability Λ and a generalized optically thick line profile [Rosmej 2012]. If also continuum radiation is important, the radiation

transport equation has to be solved. The interesting reader is refereed to [Mihalas 1978, Rosmej 2012] for further reading on these subjects.

2.2 Shocking atomic systems by XFEL radiation fields

The high peak brilliance of current/planed XFEL installations allows changing atomic populations of even highly charged ions. The coupling of the XFEL radiation to the atomic system is essentially via photo ionization and photo excitation.

2.2.1 XFEL radiation

Le us assume that time and energy dependence of the XFEL radiation are independent ($f_{FEL}(t)$ and $\tilde{N}_{FEL}(E)$, respectively) from each other. The number of photons per volume/time/energy is then given by:

$$\tilde{N}_{FEL}(E,t) = \tilde{N}_{FEL}(E) f_{FEL}(t) \tag{2.2.1}$$

$$\int_{-\infty}^{+\infty} f_{FEL}(t)dt = 1 \tag{2.2.2}$$

We assume a Gaussian energy dependence to simulate the narrow bandwidth of the XFEL:

$$\tilde{N}_{FEL}(E) = \tilde{N}_0 \frac{1}{\sqrt{\pi}\,\Gamma_{FEL}} \exp\left(-\frac{(E-E_{FEL})^2}{\Gamma_{FEL}^2}\right) \tag{2.2.3}$$

$$\Gamma_{FEL} = \delta E / 2\sqrt{\ln 2} \tag{2.2.4}$$

E_{FEL} is the central energy of the radiation field, $\tilde{N}_{FEL}(E)$ is the number of photons / volume / energy, $\tilde{N}_0$ is the peak number of photons / volume, δE is the bandwidth. Assuming a Gaussian time dependence the number of photons $N_{tot,\tau}$ per pulse length τ is given by

$$N_{tot,\tau} = \int_0^{\infty} dE \int_{volume} dV \int_{-\tau/2}^{+\tau/2} dt\, \tilde{N}_{FEL}(E,t) \approx 2Ac\tau\tilde{N}_0\, erf\left(\sqrt{\ln 2}\right) \approx 0.76Ac\tau\tilde{N}_0 \tag{2.2.5}$$

A is the focal spot area, τ is the XFEL pulse width (FWHM). The laser intensity $\tilde{I}_{FEL}(E,t)$ per bandwidth energy and time interval is related to the photon density $\tilde{N}_{FEL}(E,t)$ via

$$\tilde{I}_{FEL}(E,t)dEdAdt = \tilde{N}_{FEL}(E,t)E \cdot dEdVdt \tag{2.2.6}$$

Integrating the XFEL beam over a full width at half maximum with respect to energy and time, $\bar{I}_{FEL,\delta E,\tau}$ (energy/time/surface) is given by (assuming a Gaussian time dependence):

$$\bar{I}_{FEL,\delta E,\tau} = \int_{-\delta E/2}^{\delta E/2} dE \int_{-\tau/2}^{\tau/2} cdt\, E \cdot \tilde{N}(E,t) \approx 4E_{FEL}c\tilde{N}_0\, erf^2\left(\sqrt{\ln 2}\right) \approx 0.58 \cdot c \cdot E_{FEL} \cdot \tilde{N}_0 \tag{2.2.7}$$

or, in convenient units

$$\bar{I}_{FEL,\delta E,\tau} \approx 2.8x10^{-9}\left(\frac{\tilde{N}_0}{cm^3}\right)\left(\frac{E_{FEL}}{eV}\right)\left[\frac{W}{cm^2}\right] \tag{2.2.8}$$

The number of photons $N_{tot,\tau}$ is related to the intensity $\bar{I}_{FEL,\tau}$ via (d is the focal spot diameter)

$$\bar{I}_{FEL,\tau} = 2\cdot erf\left(\sqrt{\ln 2}\right)\cdot\frac{N_{tot,\tau}\cdot E_{FEL}}{\pi\tau\cdot d^2/4} \approx \frac{N_{tot,\tau}\cdot E_{FEL}}{\tau\cdot d^2} \tag{2.2.9}$$

2.2.2 Photo ionization

In order to change atomic populations, photo ionization rates need to be larger than corresponding electron ionization rates and, in case of photo pumping, photo excitation rates need to be larger than corresponding spontaneous radiative decay rates. In order to obtain analytical formulas, we consider a hydrogen-like atom with effective charge Z and an atomic level with principal quantum number n and energy

$$E_n = \frac{Z^2 Ry}{n^2} \tag{2.2.10}$$

where Ry = 13.6 eV. For the case of photo ionization this leads to the following relation:

$$\int_{-\tau/2}^{+\tau/2} dt \int_{E_n}^{\infty} dE\,\sigma_n^{iz}(E)\,c\,\tilde{N}_{FEL}(E,t) > n_e I_n \tag{2.2.11}$$

$\sigma_n^{iz}(E_{FEL})$ is the photo ionization cross section from level n, n_e is the electron density, I_n is the electron collisional ionization rate, c the velocity of light. Employing the Kramers classical cross section for the photo ionization

$$E > E_n : \sigma_n^{iz}(E) = 2.9\cdot 10^{-17}\frac{E_n^{5/2}}{Z\cdot E^3}\left[cm^2\right] \tag{2.2.12}$$

and the Lotz-formula for the electron collisional ionization

$$I_n = 6\cdot 10^{-8}\left(\frac{Ry}{E_n}\right)^{3/2}\sqrt{\beta_n}e^{-\beta_n}\ln\left[1+\frac{0.562+1.4\beta_n}{\beta_n(1+1.4\beta_n)}\right]\left[cm^3 s^{-1}\right] \tag{2.2.13}$$

$$\beta_n = \frac{E_n}{kT_e} \tag{2.2.14}$$

eqs. (2.2.11-2.2.14) provide the following estimate (peak intensity $I_{FEL} = cE_{FEL}\tilde{N}_0$):

$$I_{FEL} > 3\cdot 10^{-8} n_e\left(cm^{-3}\right)Z\sqrt{\beta_n}e^{-\beta_n}\ln\left[1+\frac{0.562+1.4\beta_n}{\beta_n(1+1.4\beta_n)}\right]\left[\frac{W}{cm^2}\right] \tag{2.2.15}$$

assuming $F_{EEL}=E_n+3\delta E$ ($\delta E<<E_{FEL}$) for effective photo ionization. For $n_e = 10^{21}$ cm^{-3}, Z=13, $\beta_n = 2$ eq. (2.2.15) delivers $I_{FEL} > 3x10^{13}$ W/cm^2. Let us now consider the relations for photo pumping of X-ray transitions.

2.2.3 Photo excitation

In order to influence via photo excitation on the atomic populations, photo excitation rates need to be about larger than corresponding spontaneous radiative decay rates:

$$\int_{-\tau/2}^{+\tau/2} dt \int_{\Delta E_{nm}-\delta\tilde{E}/2}^{\Delta E_{nm}+\delta\tilde{E}/2} dE\,\sigma_{nm}^{abs}(E)\,c\,\tilde{N}_{FEL}(E,t) \geq A_{mn} \tag{2.2.16}$$

$\sigma_{nm}^{abs}(E)$ is the photo absorption cross section for the transition from level n to level m and A_{mn} is the spontaneous radiative decay rate from level m to level n, $\delta\tilde{E}$ will be defined below (eq. (2.2.21)). The photo absorption cross section is given by

$$\sigma_{nm}^{abs}(E) = \frac{E}{4\pi} B_{nm}\varphi_{nm}(E) \tag{2.2.17}$$

B_{nm} is the Einstein coefficient of stimulated absorption that is related to the Einstein coefficient of spontaneous radiative decay according

$$B_{nm} = \frac{4\pi^3\hbar^3c^2}{E^3}\frac{g_m}{g_n}A_{mn} \tag{2.2.18}$$

$\varphi_{nm}(E)$ is the normalized local absorption line profile :

$$\int_{-\infty}^{+\infty} \varphi_{nm}(E)\,dE = 1 \tag{2.2.19}$$

We assume a Gaussian line profile ($FWHM = 2\sqrt{\ln 2}\,\Gamma_G$, $\Gamma_G = \Delta E_{nm}\sqrt{2kT_i / Mc^2}$ if a Doppler profile is considered) to obtain analytical estimates:

$$\varphi_{nm}(E) = \frac{1}{\sqrt{\pi}\Gamma_G}\exp\left[-\left(\frac{E-\Delta E_{nm}}{\Gamma_G}\right)^2\right] \tag{2.2.20}$$

$$\frac{4\ln 2}{\delta\tilde{E}^2} = \frac{1}{\Gamma_G^2} + \frac{1}{\Gamma_{FEL}^2} \tag{2.2.21}$$

If the XFEL photon energy is exactly tuned to the transition energy, e.g., $E_{FEL} = \Delta E_{nm}$, eqs. (2.2.3-4, 2.2.16-21) provide the following estimate:

$$I_{FEL} > 2\cdot 10^5 \Delta E_{nm}^3 \frac{g_n}{g_m}\sqrt{FWHM_{FEL}^2 + FWHM_G^2}\left[\frac{W}{cm^2}\right] \tag{2.2.22}$$

with ΔE_{nm} and FWHM in [eV]. For H-like Al Ly_α, ΔE_{nm} = 1728 eV, g_n=2, g_m=6, we obtain I_{FEL} > 4x10^{15} W/cm^2 (assuming $\sqrt{FWHM_{FEL}^2 + FWHM_G^2} = 10eV$). The relation (2.2.22) indicates an important scaling law:

$$I_{FEL} \propto Z^6 \tag{2.2.23}$$

Therefore, extremely high brilliance of XFEL's are needed to pump X-ray transitions. Assuming a spot diameter of d = 2 μm, pulse length τ = 100 fs, photon energy E_{FEL}=1.7 keV and a laser intensity of $\bar{I}_{FEL,\tau} = 10^{16} W/cm^2$, a minimum of about $N_{tot,\tau} \approx 2x10^{11}$ photons in the XFEL pulse is requested according eq. (2.2.9) to effectively move atomic populations in the X-ray energy range. Currently operating/planed Free Electron Laser facilities fulfill these requirements. As relation (2.2.22) does not depend on the electron density, the estimate for the requested XFEL intensity holds equally for low and high-density plasmas. We note that even in case of photo pumping, considerable effects on the ionic fractions take place, as collisional ionization from pumped excited states is important in dense plasmas.

2.2.4 Simulations of the interaction of XFEL with dense plasmas

Fig. 2.1 shows a principal experimental scheme for a typical pump probe experiment. A ps-ns optical laser is irradiating a solid target to create a dense plasma plume and the XFEL is used to pump X-ray transitions of ions in the plume. Corresponding simulations of the XFEL interaction with the dense plasma are carried out with the MARIA-code [Rosmej 1997, 2001, 2006] that includes all the radiation field physics described above. A detailed LSJ-split atomic atomic/ionic level system is employed to calculate the populations of different ion charge stages, ground, single and multiple excited states as well as hollow ion states.

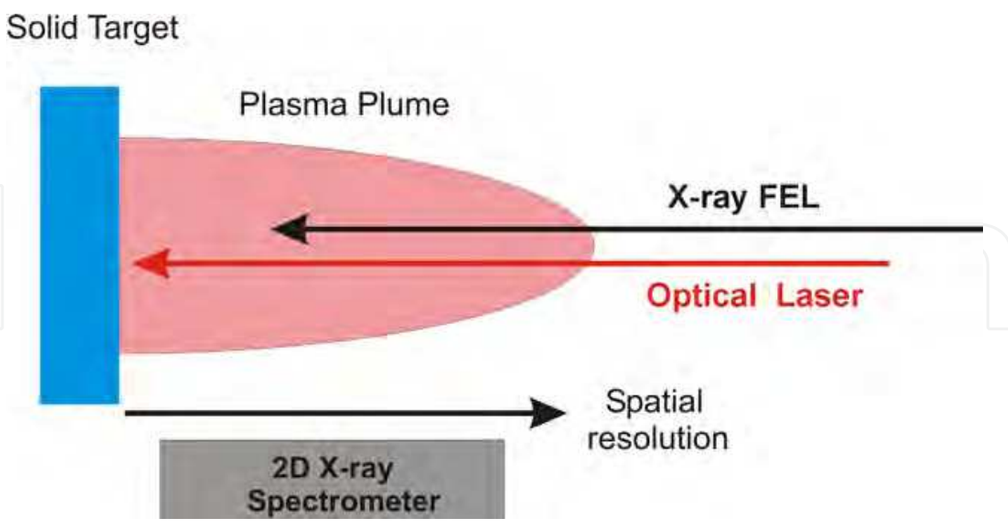

Fig. 2.1. Schematic scheme of a pump probe/photo ionization experiment. The optical laser irradiates a solid target and creates a plasma plume. The XFEL is used to pump selected X-ray transitions in the plume. A high resolution (high spectral and spatial) X-ray spectrometer is employed to record the spectral distribution of the pumped x-ray transitions and to investigate the spatial variations.

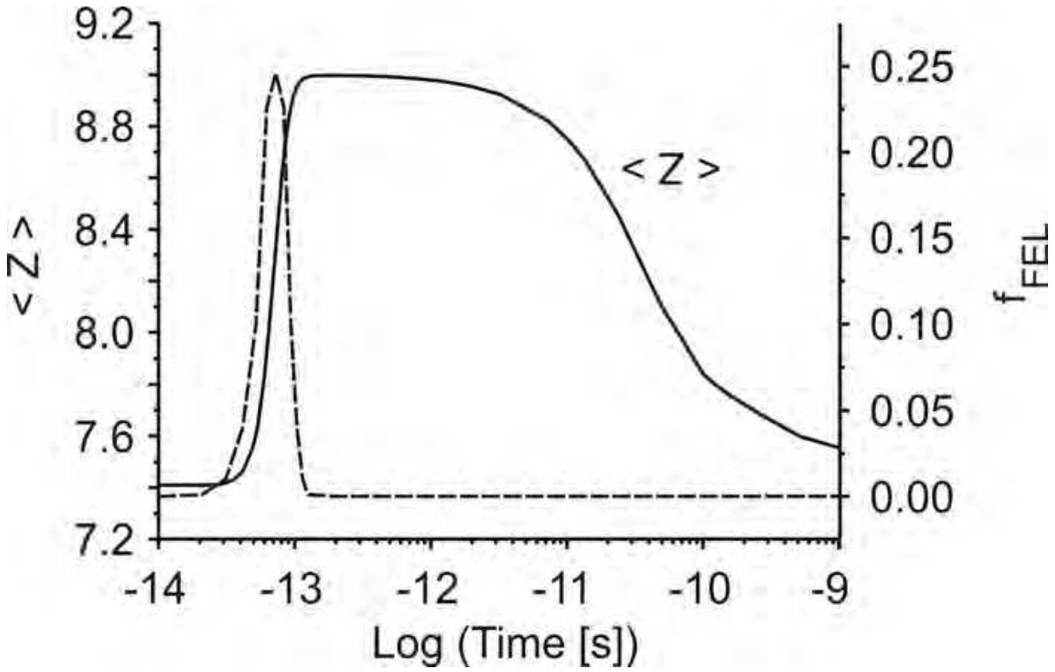

Fig. 2.2. MARIA simulations of the temporal evolution of the XFEL pulse and the average charge state of a dense Mg plasma, E_{FEL} = 1850 eV, τ=100 fs, I_{max}= 2.2x10^{17} W/cm^2, n_e = 10^{21} cm^{-3}, kT_e = 40 eV, L_{eff} = 10 μm.

Fig. 2.2 shows the evolution of the average charge (solid curve) when an intense pulsed radiation field (dashed curve) is interacting with dense magnesium plasma:

$$\langle Z \rangle = \sum_{Z=0}^{Z_n} n_Z Z \tag{2.2.24}$$

where n_z is the ionic population of charge Z (see eq. (2.1.4)). The plasma density is n_e = 10^{21} cm^{-3}, the temperature kT_e=40 eV. Opacity effects of the internal atomic/ionic radiation are included via an effective photon path length of L_{eff} = 10 μm [Rosmej 2012]. The XFEL pulse duration is τ = 100 fs, photon energy E_{FEL} = 1850 eV and the photon density is $\tilde{N}_0 = 10^{23}\, cm^{-3}$. The maximum laser intensity is related to these quantities according

$$I_{\max} = c\,E\,f_{FEL,\max}\,\tilde{N}_0 = 4.8x10^{-9}\, f_{FEL,\max}\left(\frac{\tilde{N}_0}{cm^3}\right)\left(\frac{E}{eV}\right)\left[\frac{W}{cm^2}\right] \tag{2.2.25}$$

where $f_{FEL,max}$ is the maximum value ($f_{FEL,max}$ = 0.246 in Fig. 2.2) of the normalized time dependent function of the laser intensity (see eq. (2.2.1, 2.2.2)), I_{max} = 2.2x10^{17} W/cm^2.

Before the XFEL pulse interacts with the Mg plasma plume, the average charge state is about $\langle Z \rangle \approx 7.4$ that rises dramatically during the interaction with the XFEL pulse. The system shows shock characteristics: after laser pulse maximum, the average charge state is still increasing (at about t=10^{-13} s), then stays almost constant for a few ps, then decreases on a 100 ps time scale followed by a very slow final equilibration phase (10-100 ns).

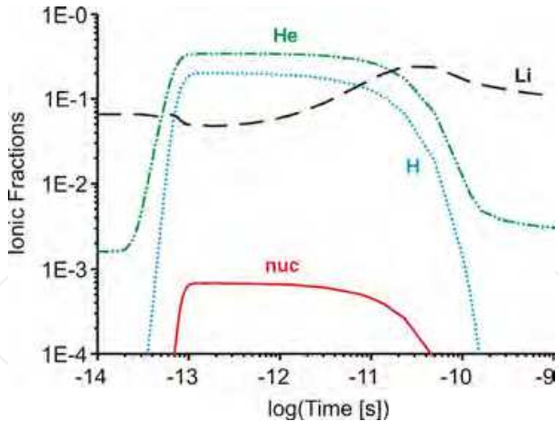

Fig. 2.3. MARIA simulations of the temporal evolution of the ionic fractions after interaction of the XFEL pulse with a dense Mg plasma plume, E_{FEL} = 1850 eV, τ=100 fs, $\tilde{N}_0 = 10^{23} cm^{-3}$, I_{max}= 2.2x10^{17} W/cm^2, n_e = 10^{21} cm^{-3}, kT_e = 40 eV, L_{eff} = 30 μm.

Let us follow the shock characteristics in more detail. Fig. 2.3 shows the charge state evolution of the bare nucleus (nuc), H-like ions (H), He-like ions (He) and Li-like ions (Li). Before the XFEL pulse the ionic fractions nuc, H and He are negligibly small due to the low electron temperature of the plasma plume. With the onset of the XFEL pulse, He-like and H-like ionic fractions rise rapidly because the photon energy E_{FEL} = 1.85 keV is larger than the ionization potential of the He-like Mg ground state ($E_i(1s^2\ ^1S_0)$ = 1762 eV).

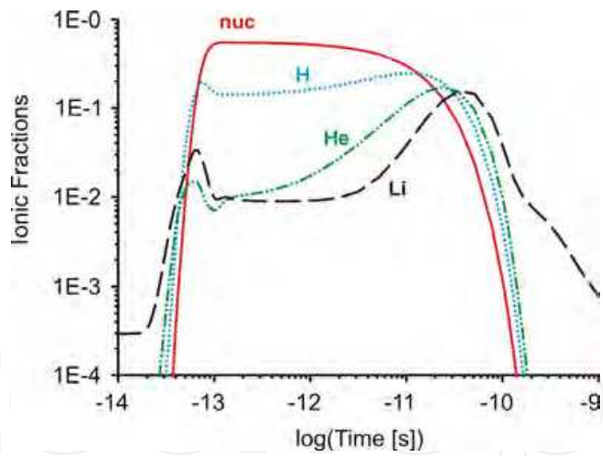

Fig. 2.4. MARIA simulations of the temporal evolution of the ionic fractions after interaction of the XFEL pulse with a dense Mg plasma plume, E_{FEL} = 3100 eV, τ=100 fs, $\tilde{N}_0 = 10^{23} cm^{-3}$, I_{max}= 3.7x10^{17} W/cm^2, n_e = 10^{21} cm^{-3}, kT_e = 30 eV, L_{eff} = 30 μm.

Fig. 2.4 shows a simulation when the photon energy is larger than the ionization potential of the H-like ground state. As in Fig. 2.3, before the XFEL pulse the ionic fractions of the bare nucleus, H- and He-like ions are negligibly small due to the low electron temperature of the plasma plume. With the onset of the XFEL pulse, Li-like, He-like and H-like ionic fractions rise rapidly. At about laser pulse maximum, the fraction of H-, He- and Li-like ions drop again because the XFEL photons are photoionizing the H-like ground state 1s $^2S_{1/2}$ because

the photon energy of E_{FEL} = 3.1 keV is larger than the ionization potential of H-like Mg ground state ($E_i(1s\ ^2S_{1/2})$ = 1963 eV). The depletion of almost all electrons from the atomic system makes the plume transparent to the XFEL radiation as no more absorption is possible: the absorption is saturated (see also paragraph 5). When the pulse is off, H-like, He-like and Li-like ionic fractions increase as recombination starts from the bare nucleus. At even later times (about t = 10^{-10} s), all ionic fractions (nuc, H, He, Li) decrease due to the overall cooling of the plume (rise of ionic fractions of low Z -ions not shown in the figures).

Figs. 2.3 and 2.4 indicate, that in the photo ionization regime, the tuning of the XFEL beam allows selection of charge states and investigation of specific shock regimes.

3. Beating the Auger-clock: Hollow crystal and hollow ion formation

3.1 Photo ionization versus autoionization

Photo ionization of inner atomic shells creates multiple excited states that can decay via non-radiative transitions. Let us consider the photo ionization from the K-shell:

$$K^2L^XM^YN^Z + h\nu_{XFEL} \rightarrow K^1L^XM^YN^Z + e_{photo} \tag{3.1.1}$$

(for example titan is described by the configuration $K^2L^8M^{10}N^2$). The photo ionized state is multiple excited and can decay via radiative and non-radiative (autoionization, known as Auger effect in solid state physics) transitions. Let us consider a simple example (Y=0, Z=0):

$$K^1L^X \rightarrow \left\{ \begin{array}{ll} radiative\,decay: & K^2L^{X-1} + h\nu_{K_\alpha} \\ non-radiative\,decay: & K^2L^{X-2} + e_{Auger} \end{array} \right\} \tag{3.1.2}$$

Radiative and non-radiative decay processes in the x-ray energy range have extensively been studied in the very past [Flügge 1957]. Particularly synchrotrons have been employed for advanced studies of X-ray interaction with solid matter. Synchrotron radiation, however, is not very intense, allowing occurrence of photo ionization of inner-shells only as a rare process (means a negligible fraction of the atoms in the crystal are photo ionized thereby leaving the solid system almost unperturbed).

This situation is quite different for XFEL's: their brilliance is more than 10 orders of magnitude higher than those of most advanced synchrotrons. Photo ionization of inner-shells may therefore concern almost every atom in the crystal structure leading to essential perturbations and corresponding dramatic changes in the physical properties (see below).

In terms of elementary processes XFEL driven photo ionization rates allow to compete even with the Auger rates (autoionizing rates Γ are very large, order of 10^{12} - 10^{16} s^{-1}). The necessary XFEL intensities to „compete" with the Auger effect can be estimated according (see also eqs. (2.2.10-2.2.12))

$$\int_{-\tau/2}^{+\tau/2} dt \int_{E_n}^{\infty} dE\, \sigma_n^{iz}(E)\, c\, \tilde{N}_{FEL}(E,t) > \Gamma \tag{3.1.3}$$

Assuming a photon energy E_{FEL} of the XFEL which is sufficient to proceed towards effective photo ionization, namely $E_{FEL} = E_n+3dE$, ($dE<<E_n$, E_n is the ionization energy of the inner shell with principal quantum number "n") we obtain the following estimate:

$$I_{FEL} > 4 \cdot 10^{-1} \cdot \Gamma \cdot \frac{Z^4}{n^3} \left[\frac{W}{cm^2} \right] \tag{3.1.4}$$

As autoionizing rates scale approximately like $\Gamma \propto Z^0$ (means almost independent of Z in the hydrogenic approximation) the Z-scaling of eq. (3.1.4) is approximately given by

$$I_{FEL} \propto Z^4 \tag{3.1.5}$$

Let us consider the photo ionization of the K-shell of Al I as an example: Z≈10.8, n=1, $\Gamma \approx 10^{14}$ s^{-1}, $I_{FEL} > 5x10^{17}$ W/cm^2.

As micro-focusing is now a standard setup at the XFEL installations, intensities in excess of 10^{17} W/cm^2 can be achieved and photo ionization of inner-shells can compete with the Auger rate. We note that this competition means that the change in atomic populations due to photo ionization is essential compared to the Auger rate that destroys the inner-shell hole.

3.2 Auger clock and hollow ion formation

Apart the threshold intensity (eq. (3.1.4) the characteristic Auger time scale is another important issue. Before XFEL's became available for dense plasma physics experiments [Rosmej & Lee 2006, 2007] proposed on the basis of simulations carried out with the MARIA code [Rosmej 1997, 2001, 2006] that "beating the Auger clock" will allow massive creation of hollow ions and permit their observation via the characteristic X-ray emission.

Let us consider the relevant physics via an example: creation of hollow ion K^0L^X-configurations and corresponding characteristic inner-shell X-ray emission. We start from the K^2L^X configurations. Photo ionization of the K-shell creates the state

$$K^2L^X + h\nu_{XFEL} \rightarrow K^1L^X + e_{photo} \tag{3.2.1}$$

In order to proceed with interesting processes from the XFEL produced single hole state K^1L^X, the duration of the XFEL pulse (being responsible for the first photo ionization) must be of the order of the characteristic Auger time scale. As planed/operating VUV/X-ray FEL facilities propose the requested pulse durations (order of 10-100 fs) photo ionization may further proceed from the single K-hole state to produce a second K-hole (hollow ion):

$$K^1L^X + h\nu_{XFEL} \rightarrow K^0L^X + e_{photo} \tag{3.2.2}$$

The existence of the double K-hole configuration K^0L^X can easily be identified via the characteristic hollow ion X-ray transitions that are located approximately between Ly_α and He_α of highly charged ions [Faenov et al. 1999]:

$$K^0L^X \rightarrow K^1L^{X-1} + h\nu_{Hollow\ ion} \tag{3.2.3}$$

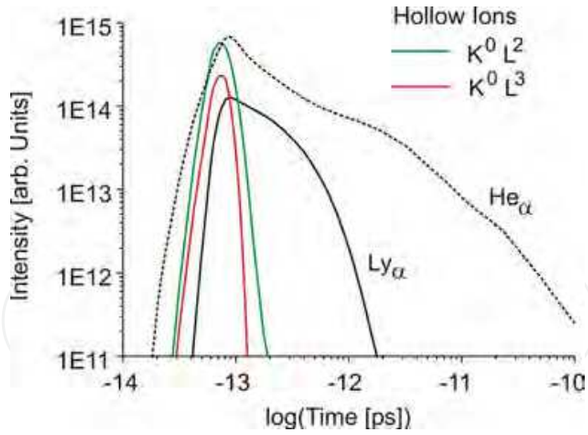

Fig. 3.1. MARIA simulations of the temporal evolution of the various line intensities after interaction of the XFEL pulse with a dense Mg plasma plume, E_{FEL} = 3100 eV, τ=100 fs, $\tilde{N}_0 = 10^{23} cm^{-3}$, I_{max} = 3.7x10^{17} W/cm^2, n_e = 10^{21} cm^{-3}, kT_e = 30 eV.

Ab initio calculations with the MARIA-code that include radiation field physics outlined in paragraph 2 demonstrate that hollow ion production is effective and observable levels of characteristic X-ray emission are achieved. These simulations have lead to a proposal for hollow ion research in dense plasmas at planed XFEL installations [Rosmej and Lee 2006].

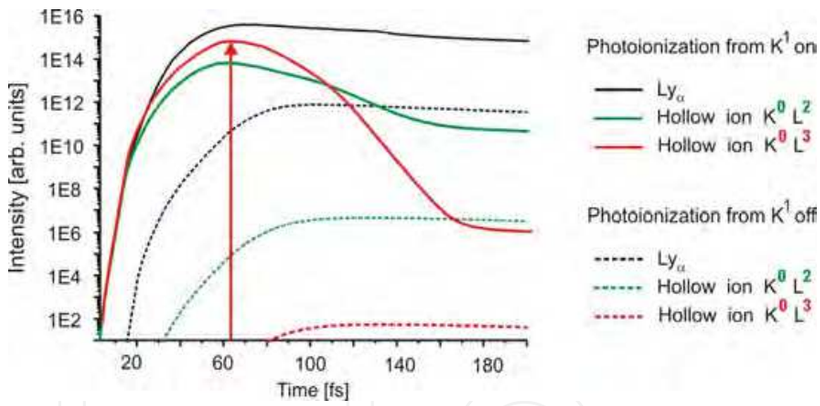

Fig. 3.2. MARIA simulations of the temporal evolution of the various line intensities after interaction of the XFEL pulse with a dense Mg plasma plume, E_{FEL} = 3100 eV, τ=100 fs, $\tilde{N}_0 = 10^{23} cm^{-3}$, I_{max} = 3.7x10^{17} W/cm^2, n_e = 10^{21} cm^{-3}, kT_e = 30 eV.

Fig. 3.1 shows the time evolution of the characteristic X-ray emission of Ly_α (2p-1s), He_α ($1s2p\ ^1P_1$-$1s^2\ ^1S_0$) as well as the X-ray emission originating from hollow ions: K^0L^2-K^1L^1 and K^0L^3-K^1L^2. The MARIA simulations have been carried out for an intense XFEL beam that is interacting with a dense Mg plasma (see Fig. 2.1) with electron density n_e = 10^{21} cm^{-3} and electron temperature kT_e = 30 eV. The photon energy is E_{FEL} = 3100 eV, pulse duration τ=100 fs and a photon density $\tilde{N}_0 = 10^{23} cm^{-3}$ (corresponding to an intensity of I_{max} = 3.7x10^{17} W/cm^2).

As can be seen from Fig. 3.1 the intensity of the hollow ion X-ray emission is of the order of the resonance line emissions (Ly_α and He_α) that are known to be observable. Let us clearly identify the real importance of the successive photo ionization for the hollow ion X-ray

emission (eqs. (3.1.1-3.1.3)). Fig. 3.2 shows the temporal evolution when all photo ionization channels are included in the simulations (solid curves) and when photo ionization from and to the states that involve a K^1-electron are artificially switched off (dashed curves in Fig. 3.2). It can clearly be seen that the hollow ion X-ray emission is practically absent when photo ionization from K^1 is off: the remaining intensities are due to collisional effects. This means that in a proof of principal simulation with the MARIA code hollow ion production and corresponding X-ray emission have been identified as driven by successive photo ionization from K^2 and K^1-electron states (see flash in Fig. 3.2). This is equivalent to say that the XFEL allows beating the Auger clock to proceed towards successive K-shell ionization before the autoionization/Auger effect disintegrates the state. We note that above-predicted double K-hole states have recently been observed [Cryan et al. 2010].

4. X-ray bursts from hollow ions and fast x-ray switches

The X-ray emission of hollow ions discussed in the forgoing paragraph provides outstanding possibilities to investigate exotic states of matter that are just produced during the XFEL pulse. Fig. 4.1 shows the temporal evolution of the hollow ion X-ray emission $K^0L^3 \rightarrow K^1L^2 + h\nu_{Hollow\ ion}$ on a linear intensity scale.

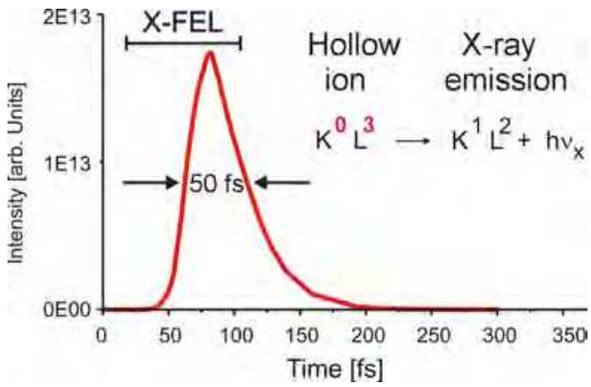

Fig. 4.1. MARIA simulations of the temporal evolution of the hollow ion X-ray emission induced by the interaction of a XFEL pulse with a dense Mg plasma plume, E_{FEL} = 3100 eV, τ=100 fs, $\tilde{N}_0 = 10^{23} cm^{-3}$, I_{max} = 3.7x10^{17} W/cm^2, n_e = 10^{21} cm^{-3}, kT_e = 30 eV.

The simulations demonstrate that the FWHM of the X-ray emission is only 50 fs and temporally located very close to the XFEL pulse. Therefore, dense matter properties that are just produced during the XFEL interaction can be studied via this X-ray emission produced by the matter itself. Moreover, we meet outstanding properties of the characteristic hollow ion X-ray emission for the K^0L^X-configurations [Rosmej et al. 2007]:

- Opacity is very small as the absorbing lower states K^1L^X are autoionizing with corresponding small populations even in dense plasmas.
- Radiative recombination effects are negligible. Therefore emission from the long lasting recombination regime at low density does not mask the high density physics during the XFEL interaction with matter. In this respect we note that particularly resonance line emission is perturbed by radiative recombination.
- Even dielectronic recombination is small as effective dielectronic caputre proceeds from ground states and not from the K^1L^X-states.

- The short time scale (some 10 fs) of the characteristic hollow ion x-ray emission acts as an effective X-ray switch that allows to study high density physics and exotic matter just after its creation by short pulse XFEL radiation. We note, that X-ray streak cameras may help to suppress emission from the recombination regime; however, they will hardly be able to streak down to 50 fs (current limits are about 0.5 ps).

5. Transparent materials and saturated absorption

A material is transparent to photons at certain energies, if neither photo absorption nor photo pumping is effective at these photon wavelengths. This is related to the density of the atomic populations: in the case of photo ionization this is the population density of the state that is photo ionized, in the case of photo pumping it is the lower state of the atomic transition that is pumped.

As has been shown in the forgoing paragraphs (eqs. (2.2.11-15), (2.2.16-22), (3.1.3-4)) XFEL radiation allows to effectively change atomic populations in the X-ray energy range. This permits to selectively deplete atomic populations. If these populations are related to photo ionization/photo pumping transparency to the XFEL radiation itself is induced and a so called "saturated absorption regime" is achieved.

Observation of saturated absorption has been claimed recently [Nagler et al. 2009] irradiating solid Al foils with a 92 eV FEL beam in the photo ionization regime:

$$1s^2 2s^2 2p^6 3s^2 3p^1 + h\nu_{XFEL} \rightarrow 1s^2 2s^2 2p^5 3s^2 3p^1 + e_{photo} \tag{5.1}$$

As photo ionization of a 2p-electron from the $2p^6$-configuration is the most effective (see eq. (2.2.12)) and a second photo ionization (means the creation of a $2p^4$-configuration) seems energetically not probable the ionization of almost all $2p^6$-configurations will induce transparence to the 92 eV XUV-laser radiation. Solid aluminum has therefore turned transparent for 92 eV photons. We note that effects of transparency are limited by the principle of detailed balance: stimulated photoemission (eq. 2.1.12) and stimulated radiative recombination (eq. 2.1.10) sets a definite limit to that what can actually be observed. Also 3-body recombination in dense matter will destroy the hole states thereby driving the saturation regime to higher intensities.

Saturated absorption implies enhanced homogeneity of the irradiated material, as no more geometrical energy deposition peaks exist. This effect is well known from the stopping of relativistic heavy ion beams in matter: if the Bragg peak is placed outside the target, almost homogenous parameter conditions are meet [Kozyreva et al. 2003, Tauschwitz et al. 2007].

The term "transparent aluminum" is also known in the non-scientific society from the science fiction series "Stark Trek" [Wiki 2011]: the chief engineer M. Scott has invented transparent aluminum to fabricate windows that have the strength and density of solid aluminum (in particular for its use to transport whales in an aquarium). This has moved XFEL research to the frontiers of science fiction [Larousserie 2009].

6. Auger electron heating

The possibility to fulfill the relations (2.2.11) and (3.1.3) on the Auger time scale allows a sudden almost maximum depletion of internal atomic shells due to photo ionization. As

almost every atom is transformed to an autoionizing state, a massive burst of Auger electrons is following.

In the x-ray energy range, the Auger electrons carry a high kinetic energy. For example, the energies of the KL-decay of the configurations $K^1L^XM^YN^Z$ are of the order of $Z^2Ry/2$, means in the keV range. As almost every atom in the crystal structure is concerned, a huge kinetic energy is released on a 10-fs time scale. This results in a rapid heating of the hollow crystal and subsequent disintegration of crystalline order followed by the creation of Warm Dense Matter and dense strongly coupled plasmas. Fig. 6.1 illustrates schematically the relevant steps in the evolution of matter after irradiation with intense XFEL radiation. We note that if the photo ionization energy is just tuned to the edge, kinetic energy of photo electrons is negligible and material heating starts from the kinetic energy of the Auger electrons.

In a proof of principle experiment Auger electron heating has been identified via high-resolution spectroscopy and introduced to the XFEL community as an important heating mechanism [Galtier et al. 2011]. We note that for optical lasers, Auger heating is irrelevant, as low photon energies are not producing holes in inner atomic shells.

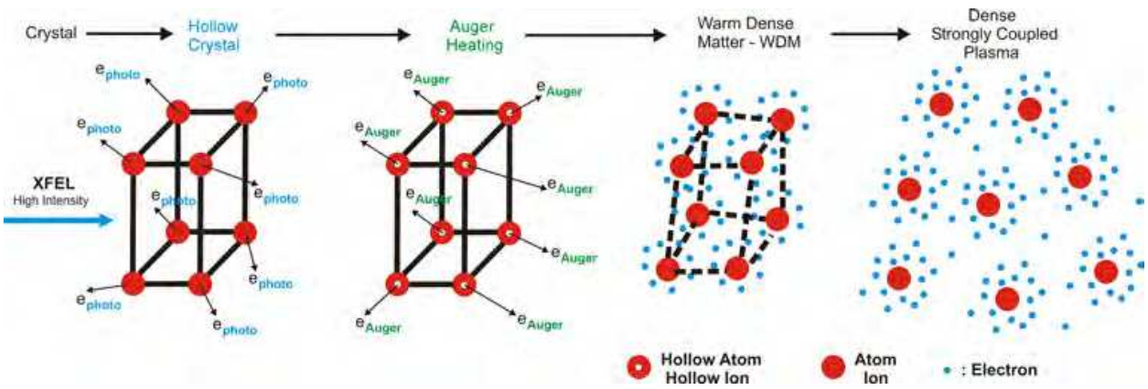

Fig. 6.1. Schematic mechanism to create hollow crystals followed by Auger electron bursts and heating, formation of Warm Dense Matter and dense strongly coupled plasmas.

In principle synchrotron radiation may produce Auger electrons via photo ionization of inner shells, however, the low intensity makes Auger emission a rare process compared to the huge number of atoms that are not concerned (note, that this is not a contradiction to the fact that Auger electron spectra can be well measured). Therefore no heating of the crystal is induced. Moreover, synchrotron radiation does not allow photo ionization on the Auger time scale and is therefore in principle not able to create exotic states of matter such as "hollow crystals", "transparent solids" etc.

7. Hole states in dense plasmas and Excited Sates Coupling (ESC) effects

7.1 Re-creation of hole states in dense plasmas after hollow crystal formation

First principles predict a re-population of hole states after photo ionization at times when the hollow crystal turns to a dense strongly coupled plasma, see Fig. 6.1. The principle of micro-reversibility that is based on the CPT-invariance of the Hamiltonian [e.g. Dawydow 1981] requests that autoionization is followed by its inverse process (inverse Auger or dielectronic capture):

$$D_{jk} = \frac{\pi^2}{\sqrt{2}} \frac{\hbar^3}{m_e^{3/2}} \frac{g_j}{g_k} \frac{\Gamma_{jk}}{\sqrt{E_{jk}}} F\left(E_{jk}, E\right) \tag{7.1.1}$$

D_{jk} is the dielectronic capture from state k to the autoionizing state j, Γ_{jk} is the corresponding autoionization rate, E_{jk} is the dielectronic capture energy, g_j and g_k are the statistical weights of states j and k, $F(E_{jk}, E)$ is the electron energy distribution function. In order to proceed with analytical estimates, let us assume that collisions between the Auger electrons are so frequent that a Maxwellian electron energy distribution is quickly established (fs-time scale):

$$D_{jk} = \frac{(2\pi)^{3/2}\hbar^3}{2m_e^{3/2}} \frac{g_j}{g_k} \Gamma_{jk} \frac{\exp\left(-E_{jk}/kT_e\right)}{\left(kT_e\right)^{3/2}} = 1.656 \cdot 10^{-22} \frac{g_j \Gamma_{jk}}{g_k} \frac{\exp\left(-E_{jk}(eV)/T_e(eV)\right)}{\left(T_e(eV)\right)^{3/2}} \frac{cm^3}{s} \tag{7.1.2}$$

As discussed in paragraph 6, capture energies are of the order of $Z^2Ry/2$ implying that in a regime of saturated absorption where almost every atom is accompanied by an Auger electron, the electron temperature is expected to be of similar order (note, that after autoionization Auger electron kinetic energy is redistributed amongst the remaining electrons; for metals the electrons in the conduction band). Therefore the exponential factor in eq. (7.1.2) is not small and the inverse Auger effect that is effectively re-creating hole states in a dense plasma (see also Fig. 6.1) can be detected via the characteristic X-ray emission.

7.2 Excited States Coupling (ESC) of inverse Auger effect

In atomic physics, the characteristic X-ray emission of hole states is known as dielectronic satellite emission that is of considerable importance to study dense plasmas physics via independent (from plasma simulations) diagnostics of temperature, density, charge states, supra-thermal electrons, non-equilibrium effects etc. The interesting reader is refereed to the reviews of [Boiko et al. 1985, Rosmej 2012] for further reading on this subject.

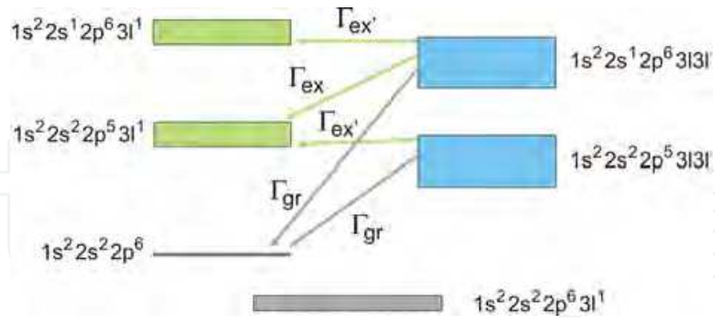

Fig. 7.1. Schematic energy level diagram of Al III and Al IV including hole states. Possible autoionization channels to ground and excited states are indicated.

In a dense plasma (Fig. 6.1) the inverse Auger effect is not only related to the original state "k" (see eq. (7.1.1)) but to excited states too. This can entirely change the picture of the inverse Auger effect. We illuminate excited state effects with an example: L-shell photo ionization of singly ionized aluminum ($K^2L^8M^2$-configuration). Photo ionization creates the autoionizing state j = $K^2L^7M^2$ that decays towards k = K^2L^8. The principle of micro-reversibility predicts therefore dielectronic capture according $K^2L^8 + e \rightarrow K^2L^7M^2$.

In dense plasmas, however, excited states are strongly populated via electron collisional excitation: $K^2L^8 + e \rightarrow K^2L^7M^1 + e$. This opens up the possibility to proceed towards dielectronic capture from excited states if the energy level structure energetically does permit this channel [Rosmej et al. 1998]. The so called "Excited States Coupling - ESC" changes almost all properties of the radiation emission and even overall satellite intensity by itself is not anymore related to the fundamental exponential factor of eq. (7.1.2).

	$1s^22s^22p^53l3l'$	$1s^22s^12p^63l3l'$
$1s^22s^22p^6$	$2.2x10^{12}$	$1.1x10^{12}$
$1s^22s^22p^53l$	$2.1x10^{13}$	$5.4x10^{14}$
$1s^22s^12p^63l$	-	$2.1x10^{13}$

Table 7.1. Averaged autoionzing rates Γ in [s^{-1}] of Al III related to ground and excited states.

In order to illuminate the situation, let us consider the relevant energy level diagram of Al III and Al IV in more details, Fig. 7.1. It can be seen that the levels $1s^22s^12p^63l3l'$ are not only coupled to the ground state $1s^22s^22p^6$ (Γ_{gr}) but to excited states $1s^22s^22p^53l$ too (Γ_{ex}) and even partially to the states $1s^22s^12p^63l$ ($\Gamma_{ex'}$). Similar relations hold true for the $1s^22s^22p^53l3l'$-levels: ground state coupling and partially excited states $1s^22s^22p^53l$ ($\Gamma_{ex'}$) coupling.

	$1s^22s^22p^53l3l'$	$1s^22s^12p^63l3l'$
$1s^22s^22p^63l$	$3.8x10^9$	$2.4x10^9$
$1s^22s^22p^53l31'$	-	$4.1x10^{10}$

Table 7.2. Averaged spontaneous radiative decay rates A in [s^{-1}] of Al III.

Table 7.1 illustrates that autoionizing rates from excited states are even more important than those from ground states: about 1-2 orders of magnitude. Table 7.2 shows the relevant spontaneous radiative decay rates that are 2-5 orders of magnitude smaller than autoionizing rates. The statistically averaged data in tables 7.1-2 have been calculated with the FAC code [Gu 2008] employing a multi-configuration relativistic atomic structure, fine structure (LSJ-split levels), intermediate coupling and configuration interaction.

The data depicted in tables 7.1 and 7.2 imply that characteristic line emission from hole states that are produced by dielectronic capture from the ground state are barely visible due to a non-favorable branching factor for spontaneous radiative emission:

$$B_{ji} = \frac{A_{ji}}{\sum_i A_{ji} + \sum_k \Gamma_{jk}} \tag{7.2.1}$$

In dense plasmas, however, the excited states are strongly populated and dielectronic capture may proceed from excited states (also the branching factor is modified by collisions). In this case, quite different relations are encountered for characteristic emission of hole states. In a single level approximation, the line intensity is given by

$$I_{ji}\left(K^2L^7M^2\right) = n_e n\left(K^2L^8\right)B_{ji}D_{j,K^2L^8} + \sum_{K^2L^7M^1} n_e n\left(K^2L^7M^1\right)B_{ji}D_{j,K^2L^7M^1} \tag{7.2.2}$$

As the excited states autoionizing rates are much larger than the radiative decay rates and the ground state autoionizing states, the first term in eq. (7.2.2) almost vanishes. The second term is almost independent of the autoionzing rates as the branching factor multiplied with the excited state autoionizing rate is of the order of 1:

$$I_{ji}\left(K^2L^7M^2\right) \approx \sum_{K^2L^7M^1} n_e n\left(K^2L^7M^1\right) A_{ji} \frac{2^{3/2}\pi^{3/2}\hbar^3}{2m_e^{3/2}} \frac{g_j}{g_{K^2L^7M^1}} \frac{\exp\left(-E_{j,K^2L^7M^1} / kT_e\right)}{\left(kT_e\right)^{3/2}} \quad (7.2.3)$$

The dependence on the excited state density n($K^2L^7M^1$) implies that the intensity (eq. (7.2.3)) depends strongly on the electron density and not only on temperature as originally proposed by [Gabriel 1972].

This is demonstrated with simulations of the characteristic line emission from $K^2L^7M^2$ hole states together with the corresponding resonance line emission $K^2L^7M^1$-K^2L^8, Fig. 7.2. Simulations have been carried out employing all LSJ-split levels of the K^2L^8-configuration (1 level), $K^2L^7M^1$-configuration (36 levels), $K^2L^8M^1$-configuration (5 levels) and the $K^2L^7M^2$-configuration (237 levels) and including intermediate coupling and configuration interaction. Corresponding atomic population kinetics include electron collisional excitation/de-excitation, ionization/three body recombination, spontaneous radiative decay, autoionization and dielectronic capture [Rosmej et al. 2011].

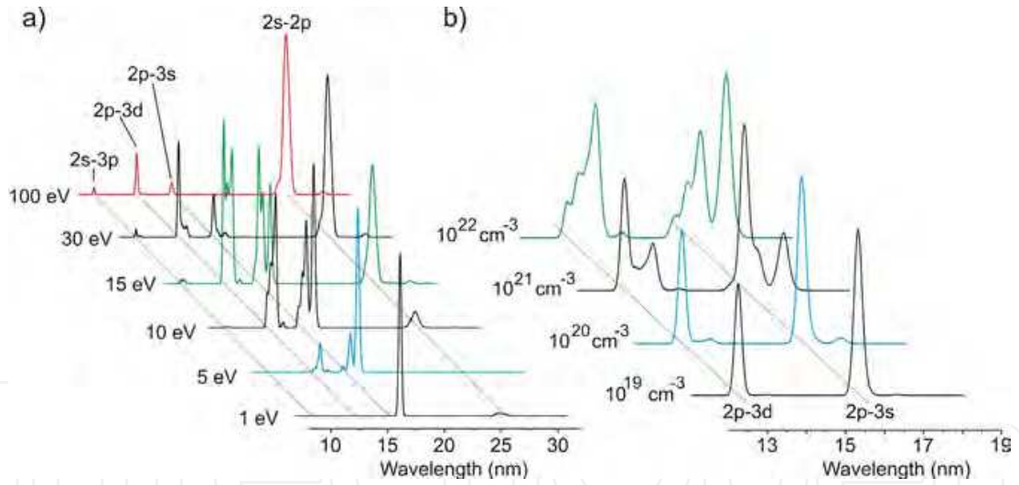

Fig. 7.2. a) Simulations of the spectral emission of Al IV and Al III emission (normalized to peak), a) temperature dependence, $n_e = 10^{22}$ cm^{-3}, b) density dependence, $kT_e = 10$ eV.

Fig. 7.2a shows the electron temperature dependence of the spectral distribution (see eq. (2.1.14)). The dashed lines indicate the positions of the resonance transitions in Al IV (2s-3p, 2p-3d and 2p-3s) as well as the intra-shell transitions (2s-2p). Other spectral features are due to the characteristic line emission of hole states originating from the $K^2L^7M^2$-configuration. Two observations can be made: first, with increasing electron temperature, the intensity of the intra-shell transition rises considerably, second, strong satellite emission is observed for temperatures around 15 eV. For very low electron temperatures (e.g., 1 eV in Fig. 7.2a), the line emission consists only from satellite transitions (note, however, that absolute line intensity is very low making experimental observation rather difficult). Fig. 7.2b shows the

spectral range near the resonance transitions 2p-3d and 2p-3s (indicated by dashed lines) for different electron densities, other emission features are due to characteristic line emission from the hollow ion configuration $K^2L^7M^2$. At low electron densities, $n_e = 10^{19}$ cm^{-3}, satellite emission is barely visible. With increasing electron density, the satellite emission rises considerably due to excited state coupling effects (see discussion of eq. (7.2.3)).

We note, that also collisional redistribution between the autoionizing levels leads to intensity changes of the spectral distribution of satellite transitions (included in the present simulations), however, this concerns essentially deformations of the spectral distribution [Rosmej 2012] and not an overall drastic intensity increase as observed in Fig. 7.2b.

With respect to the overall temporal evolution of matter irradiated by XFEL radiation (Fig. 6.1), Fig. 7.2 demonstrates (see curve for $n_e = 10^{22}$ cm^{-3}) that the characteristic line emission from hole states might be even more important than usual resonance line emission. Satellite emission plays therefore an exceptional role to explore radiative properties of high density matter under extreme conditions.

8. Quantum mechanical interference effects

8.1 Pumping characteristic X-ray transitions in autoionizing hole states

Let us now consider novel effects in the spectral line broadening of characteristic X-ray line emission from hole states. The newly emerging XFEL installations will permit outstanding observations of quantum mechanical interference effects as the XFEL can be employed to directly pump the characteristic x-ray emission in dense matter.

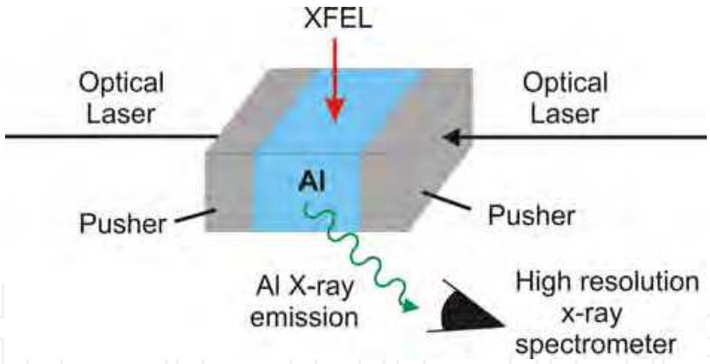

Fig. 8.1. Schematic experimental pump-probe scheme to investigate quantum mechanical interference effects in near and above (compressed) solid density matter with X-ray Free Electron Lasers and high resolution X-ray spectroscopy.

A principle experimental scheme is depicted in Fig. 8.1. The radiating test element (Al in Fig. 8.1) is compressed with optical laser beams. When the matter is effectively compressed a 100 fs XFEL pulse will further heat the compressed matter (e.g., Auger electron heating and photo electron heating, see paragraph 6) and pump X-ray transitions by effective wavelength tuning. Let us consider hole states in Li-like ions. The XFEL frequency is adjusted in such a way to pump X-ray transitions from the Li-like states $1s^22l$ to excite the multiple excited states $1s2l2l'$: $1s^22l + h\nu_{XFEL} - 1s2l2l'$. After excitation, the soft x-ray emission $1s2l2l' - 1s^22l' + h\nu_{satellites}$ is observed with a high-resolution x-ray spectrometer.

The short time scale of the X-ray pump provides practically a snap shot of the parameter situation thereby avoiding too many complications due to time integration. The pumping of the satellite transitions has namely the great advantage of extremely short time scale for the radiation emission itself because the relevant characteristic emission time $\tau_{eff,j}$ of a certain autoionizing atomic level "j" is not given by the spontaneous transition probabilities but rather by the sum of autoionizing and radiative decay rates [Rosmej 2012]:

$$\tau_{eff,j}^{-1} \approx \sum_i A_{ji} + \sum_k \Gamma_{jk} \tag{8.1.1}$$

For the 1s2l2l'-satellites of Al, the strongest radiative decay and autoionizing rates are of the order of $1x10^{13}$ s^{-1} and $1x10^{14}$ s^{-1}, respectively, implying effective response times of the order of $\tau_{eff}(1s2l2l') \approx 10$ - 100 fs. Even for 1s2l3l'-satellites we encounter very fast response times: the strongest radiative decay and autoionizing rates are of the order of $2x10^{13}$ s^{-1} and $3x10^{13}$ s^{-1}, respectively, implying $\tau_{eff}(1s2l3l') \approx 30$ - 500 fs. Therefore, time integration effects due to characteristic photon emission times are very small as τ_{eff} is smaller than hydrodynamic time scales.

8.2 Line broadening and interference effects of hollow ion X-ray emission

Spectral line broadening that is due to the interaction of a radiating atom with surrounding particles is closely connected with the theory of atomic collisions and extensive reviews have been published on this issue [e.g., Griem 1974, 1997, Sobelman et al. 1995].

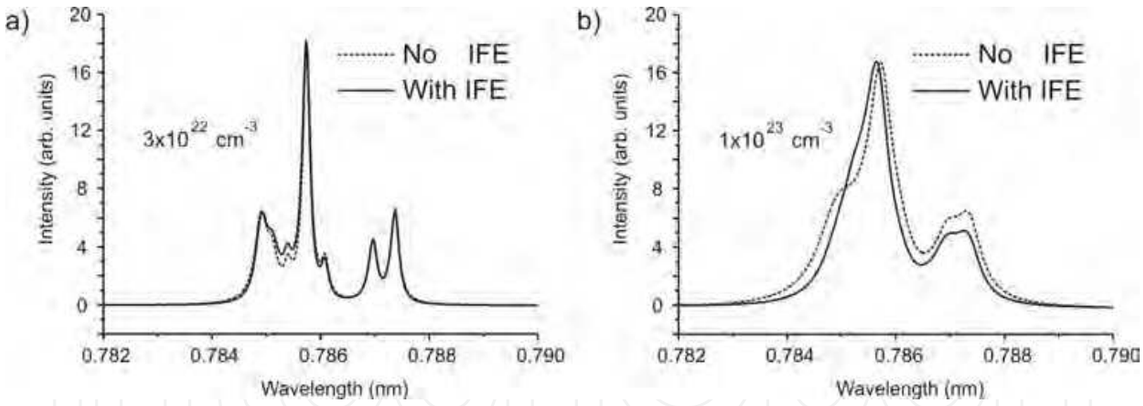

Fig. 8.2. Onset of interference effects (IFE) in dielectronic satellite transitions 1s2l2l'-1s2l' + hν of Li-like aluminum, a) $n_e = 3x10^{22}$ cm^{-3}, $kT_e = 100$ eV, b) $n_e = 1x10^{23}$ cm^{-3}, $kT_e = 100$ eV.

The general theory of impact broadening is based on the density matrix and quantum kinetic approach and considers the scattering amplitudes and phases thereby allowing to consider quantum mechanical interference effects. In the line broadening theory, interference effects arise due to transition frequencies that coincide or are so closely spaced that the corresponding spectral lines overlap. In some cases, the interference effects are so important that they alter the entire picture of the line broadening and it has been noted long time ago that interference effects may lead to a considerable line narrowing [Aleseyev and Sobelman 1969, Sobelman et al. 1995].

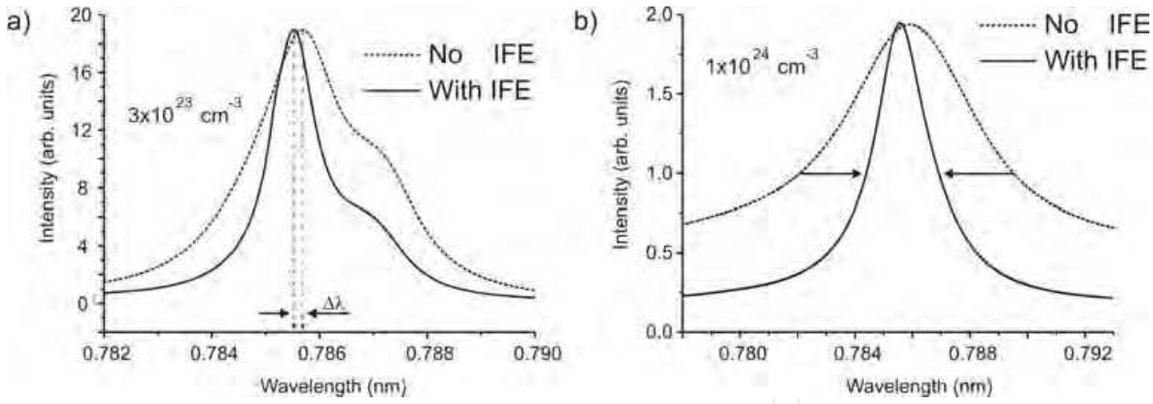

Fig. 8.3. Strong interference effects (IFE) in dielectronic satellite transitions 1s2l2l′-1s2l′ + hν of Li-like aluminum, a) $n_e = 3x10^{23}$ cm^{-3}, $kT_e = 100$ eV, b) $n_e = 1x10^{24}$ cm^{-3}, $kT_e = 100$ eV. Interference effects lead to a considerable line narrowing (see arrows in (b)) and also to wavelengths shift Δλ (see (a)) of the emission group.

In order to apply Stark broadening to real experimental conditions, opacity broadening and sensitivity to a low density recombination regimes has to be avoided: this is difficult employing resonance lines of H- and He-like ions. Moreover, as the respective ground states are the states 1s $^2S_{1/2}$ and 1s^2 $^1S_0$, interference effects do not arise. All these problems are circumvented employing the dielectronic statellite transitions to Ly_α of He-like ions 2lnl′ - 1snl′ + $h\nu_{sat}$ and to He_α of Li-like ions 1s2lnl′ - 1s^{2}nl′ + $h\nu_{sat}$ (one the most frequently used transitions to diagnose hot dense plasmas [Rosmej 2012]). As lower states are numerous interference effects can arise. Moreover, their short emission times scales (see discussion of eq. (8.1.1)) confines the emission near the XFEL interaction times where density is highest. We note that optical laser produced plasmas suffer from limited plasma density (order of the critical densities) and the experimental scheme depicted in Fig. 8.1 will be extremely challenging to probe near and above (compressed) solid density matter by XFEL pumping.

Stark broadening calculations of the characteristic line emission that originate from hollow ions involves very complex configurations with the corresponding need to calculate millions of Stark transitions. At present, one of the most general and powerful methods to calculate line profiles for such complex transitions has been developed with the PPP-code that is based on the frequency fluctuation model [Talin et al. 1995, Calisti et al. 2006, 2010]. PPP allows rapid Stark broadening calculations of millions of Stark transitions and includes the possibility to calculate ion dynamics and interference effects.

Fig. 8.2 shows the Stark broadening simulations carried out with the PPP-code for the dielectronic satellite transitions of Li-like Al: 1s2l2l′ - 1s^{2}2l′ + $h\nu_{sat}$. We note that for the present calculations the requested dipole matrix elements do include configuration interaction, intermediate coupling and LSJ-split level structure. In order not to mask interference effects with population kinetic effects, a statistical population between the levels has been employed. The curves in Fig. 8.2a are calculated for an electron density of $n_e = 3x10^{22}$ cm^{-3} without (dashed curve) and with (solid curve) interference effects (IFE). It can be seen, that interference effects are barely visible at these electron densities. At $n_e = 1x10^{23}$ cm^{-3} interference effects start to show up.

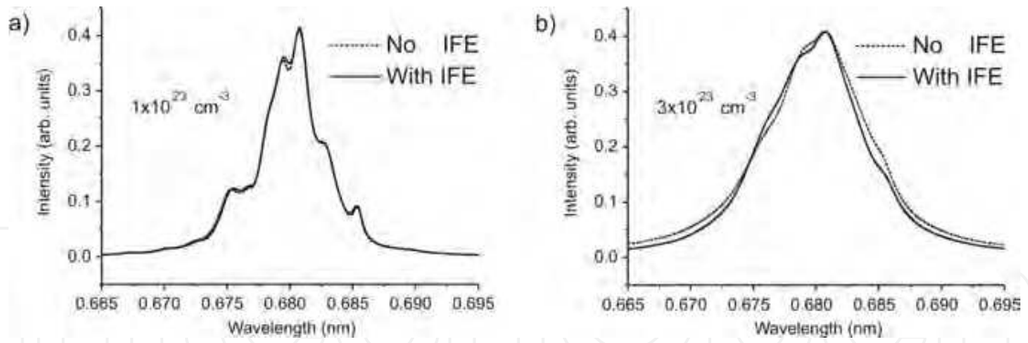

Fig. 8.4. Investigation of interference effects (IFE) in dielectronic satellite transitions $1s2l3l' - 1s^22l + h\nu$ of Li-like aluminum near He_β, a) $n_e = 1x10^{23}$ cm^{-3}, $kT_e = 100$ eV, b) $n_e = 3x10^{23}$ cm^{-3}, $kT_e = 100$ eV. Interference effects lead only to small changes in the overall spectral distribution.

Figure 8.3 shows parameters, where strong interference effects are expected. At $n_e = 3x10^{23}$ cm^{-3} IFE result in a serious narrowing of the emission group and also to a qualitative distortion of the spectral distribution. Also a strong wavelength shift of the emission group (indicated by the peak center shift $\Delta\lambda$ in Fig. 8.3a) is observed. At even higher densities, $n_e = 3x10^{23}$ cm^{-3} IFE have reduced the overall width of the emission group by a factor of 2-3 (see arrows in Fig. 8.3b). This indicates that Stark broadening simulations that do not include IFE considerably underestimate the electron density when applied to experimental data.

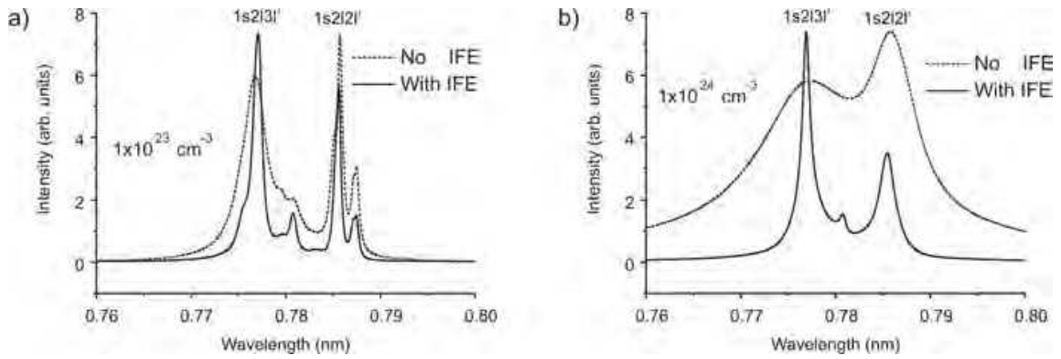

Fig. 8.5. Investigation of interference effects (IFE) in dielectronic satellite transitions $1s2l3l' - 1s^23l' + h\nu$ of Li-like aluminum near He_α, a) $n_e = 1x10^{23}$ cm^{-3}, $kT_e = 100$ eV, b) $n_e = 1x10^{24}$ cm^{-3}, $kT_e = 100$ eV. Interference effects lead to large changes in the overall spectral distribution.

As the XFEL radiation can equally be tuned to the β-transitions it is quite challenging to look for the Li-like satellite transitions $1s2l3l' - 1s^22l + h\nu_{He\beta\text{-sat.}}$ near the He_β resonance line (He_β = $1s3p\ ^1P_1 - 1s^2\ ^1S_0$): broadening effects are expected to be visible for lower densities (as compared to the 1s2l2l'-satellites) and opacity effects are even more reduced. Fig. 8.4 shows the corresponding simulations. As can be seen from Fig. 8.4a/b, interference effects lead only to rather small changes in the overall spectral distribution. The reason for these rather small effects is connected with the relatively limited number of lower states ($1s^22l'$-configuration). The situation is dramatically different when considering interference effects of the 1s2l3l'-satellites near He_α ($1s2p\ ^1P_1 - 1s^2\ ^1S_0$): $1s2l3l' - 1s2nl' + h\nu_{He\alpha\text{-sat.}}$ (lower states $1s^23l'$). Fig. 8.5 shows the corresponding simulations. Dramatic changes in the overall spectral distribution are observed, in particular, interference effects lead to a considerable

shape narrowing of the group emission. We note that the simulations of Fig. 8.5 are rather complex involving the calculation of some 10 million Stark transitions.

The dramatic difference of the interference effects of He_α- and He_β-satellites (see Figs. 8.4 and 8.5) originating from 1s2l3l'-configurations allows direct experimental verification: the negligible interference effects in the He_β-satellites serve as an experimental reference broadening allowing to detect the group narrowing due to interferences in the 1s2l3l' He_α-satellites. In this respect we note, that high resolution X-ray spectroscopy has proven to provide sufficient resolution to separate the 1s2l3l' He_α-satellites from the He_α-resonance line itself even in dense laser produced plasmas [Rosmej et al. 1998]. Also observable line intensities are expected as successful pumping of Li-like satellite transitions in a dense plasma plume has already been demonstrated in recent experiments at the LCLS [LCLS 2011] XFEL facility [Seely et al. 2011].

The XFEL pumping of characteristic X-ray transitions in hollow ions provides therefore outstanding experimental conditions to study novel high-density matter physics. : first, the pump allows selectively increasing the satellite transitions to obtain good signal to noise ratio, second, the short time scale (of XFEL pump and satellite transitions itself) avoids ambiguities due to time integration effects (integration over different plasma parameters during evolution).

9. Conclusion

High intensity short pulse XUV/X-FEL Free Electron Laser radiation provides to the scientific community outstanding tools to investigate matter under extreme conditions never obtained in laboratories so far. We have presented novel effects in the solid-to-plasma transition considering irradiation of solid matter with high intensities and short XUV/XFEL pulses. Exotic states of matter such as transparent metals, hollow crystals and X-ray bursts from hollow ions have been investigated. Novel effects in atomic physics have been studied: Auger electron bursts from hollow crystals, 10-fs atomic X-ray switches, excites states coupling effects induced by dense matter and quantum mechanical interference effects in the characteristic X-ray line emission from hole states.

A new heating mechanism was discussed: "Auger electron heating" followed by the decay of crystalline order, formation of Warm Dense Matter and strongly coupled plasmas. Finally we have explored the exceptional role of characteristic X-ray emission (satellites) from hole states/hollow ions to study radiative properties of dense matter under extreme conditions.

10. Acknowledgment

Support from the project "Èmergence-2010: *Métaux transparents créés sous irradiations intenses émises par un laser XUV/X à électrons libres*" of the University Pierre and Marie Curie and the "Extreme Matter Institut - EMMI" are greatly appreciated.

11. References

Aleseyev, V.A. & Sobelman, I.I. (1969). *Influence of Collisions on Stimulated Random Scattering in Gases,* JETP 28, 991.

Boiko, V. A.; Vinogradov, A. V.; Pikuz, S. A.; Skobelev, I. Yu. & Faenov, A. Ya. (1985). *X-ray spectroscopy of laser produced plasmas*, J. Sov. Laser Research 6, 82.

Calisti, A.; Ferri, S.; Mossé-Sabonnadière, C. & Talin, B. (2006). *Pim Pam Pum,* Report Université de Provence, Marseille, France.

Calisti, A.; Galtier, E.; Rosmej, F.B.; Ferri, S.; Mossé, C.; Talin, B. & Lisitsa, V.S. (2010). *Detailed Stark calculations of aluminum emission from hole states induced by XUV-Free Electron Laser irradiations*, 14th International Workshop on Radiative Properties of Hot Dense Matter (4-8/10/2010), Marbella, Spain.

Cryan, J.P.; Glownia, J. M.; Andreasson, J.; Belkacem, A.; Berrah, N.; Blaga, C.I.; Bostedt, C. Bozek, J.; Buth, C.; DiMauro, L.F.; Fang, L.; Gessner, O.; Guehr, M.; Hajdu, J.; Hertlein, M.P.; Hoener, M.; Kornilov, O.; Marangos, J.P.; March, A.M.; McFarland, B. K.; Merdji, H.; Petrovic´, V.S.; Raman, C.; Ray, D.; Reis, D.; Tarantelli, F.; Trigo, M.; White, J. L.; White, W.; Young, L.; Bucksbaum, P.H. & Coffee, R.N. (2010). *Auger Electron Angular Distribution of Double Core-Hole States in the Molecular Reference Frame*, Phys. Rev. Lett. 105, 083004.

Dawydow, A.S. 1981. *Quantenmechanik*, VEB Deutscher Verlag der Wissenschaften, Berlin.

Faenov, A.Ya.; Magunov, A.I.; Pikuz, T.A.; Skobelev, I.Yu.; Pikuz, S.A. ; Urnov, A.M.; Abdallah, J.; Clark, R.E.H.; Cohen, J.; Johnson, R.P. ; Kyrala, G.A.; Wilke, M.D.; Maksimchuk, A.; Umstadter, D.; Nantel, R. Doron, N.; Behar, E.; Mandelbaum, P.; Schwob, J.J.; Dubau, J. ; Rosmej, F.B. & Osterheld, A. 1999. *High-Resolved X-Ray Spectra of Hollow Atoms in a Femtosecond Laser-Produced Solid Plasma*", Physica Scripta T80, 536 (1999).

Flügge, E. (1957). *Encyclopedia of Physics*, vol. XXX (X-rays), Springer.

Gabriel, A.H. 1972. *Dielectronic satellite spectra for highly charged He-like ion lines*. Mon. Not. R. astro. Soc. 160, 99.

Galtier, E.; Rosmej, F.B.; Riley, D.; Dzelzainis, T.; Khattak, F.Y.; Heimann, P.; Lee, R.W.; Vinko, S.M.; Whitcher, T.; Nagler, B.; Nelson, A.; Wark, J.S.; Tschentscher, T.; Toleikis, S.; Fäustlin, R.; Sobierajski, R.; Jurek, M.; Juha, L.; Chalupsky, J.; Hajkova, V.; Kozlova, M. & Krzywinski, J. (2011). *Decay of cristaline order and equilibration during solid-to-plasma transition induced by 20-fs microfocused 92 eV Free Electron Laser Pulses*, Phys. Rev. Lett. 106, 164801.

Griem, H.R. (1974). *Specral Line Broadening by Plasma*, Academic Press, New York.

Griem, H.R. (1997). *Principles of Plasma Spectroscopy*, Cambridge University Press, New York, ISBN 0-521-45504-9.

Gu, M.F. 2008. The flexible atomic code FAC, Canadian Journal of Physics 86 (5), 675.

Kozyreva, A.; Basko, M.; Rosmej, F.B.; Schlegel, T.; Tauschwitz, A. & Hoffmann, D.H.H. (2003). *Dynamic confinement of targets heated quasi-isochorically with heavy ion beam*, Phys. Rev. E 68, 056406.

Larousserie, D. 2009. *L'aluminium devient transparent aux rayons X*. Science et Avenir, vol. 09/2009, p. 20.

LCLS 2011. http://www-ssrl.slac.stanford.edu/lcls/

Loudon, R. (2000). *The quantum theory of light*, Oxford University Press, New York, ISBN 0-19-8501767-3.

Mihalas, D. 1978. *Stellar Atmospheres*, W.H. Freeman, San Francisco, 2nd edition.

Nagler, B.; Zastrau, U; Fäustlin, R; Vinko, S.M.; Whitcher, T.; Nelson, A. J.; Sobierajski, R.; Krzywinski, J.; Chalupsky, J.; Abreu, E.; Bajt, S.; Bornath, T.; Burian, T.; Chapman, H.; Cihelka, J.; Döppner, T.; Düsterer, S.; Dzelzainis, T.; Fajardo, M.; Förster, E.;

Fortmann, C.; Galtier, E.; Glenzer, S. H.; Göde, S.; Gregori, G.; Hajkova, V.; Heimann, P.; Juha, L.; Jurek, M.; Khattak, F.Y.; Khorsand, A.R.; Klinger, D.; Kozlova, M.; Laarmann, T.; Lee, H.J.; Lee, R.W.; Meiwes-Broer, K.-H.; Mercere, P.; Murphy, W.J.; Przystawik, A.; Redmer, R.; Reinholz, H.; Riley, D.; Röpke, G.; Rosmej, F.B.; Saksl, K.; Schott, R.; Thiele, R.; Tiggesbäumker, J.; Toleikis, S.; Tschentscher, T.; Uschmann, I.; Vollmer, H. J. & Wark, J. (2009). *Transparency induced in solid density aluminum by ultra-intense XUV Radiation*, Nature Physics 5, 693.

Rosmej, F.B. (1997). *Hot Electron X-ray Diagnostics*, J. Phys. B. Lett.: At. Mol. Opt. Phys. 30, L819.

Rosmej, F.B.; Faenov, A.Ya.; Pikuz, T.A.; Flora, F.; Lazzaro, P. Di; Bollanti, S.; Lizi, N.; Letardi, T.; Reale, A.; Palladino, L.; Batani, O.; Bossi, S.; Bornardinello, A.; Scafati, A. & Reale, L. (1998). *Line Formation of High Intensity He_b-Rydberg Dielectronic Satellites 1s3lnl' in Laser Produced Plasmas*, J. Phys. B Lett.: At. Mol. Opt. Phys. 31, L921.

Rosmej, F.B. (2001). "*A new type of analytical model for complex radiation emission of hollow ions in fusion and laser produced plasmas*", Europhysics Letters 55, 472.

Rosmej, F.B. (2006). *An alternative method to determine atomic radiation"*, Europhysics Letters 76, 1081.

Rosmej, F.B. & Lee, R.W. (2006). *Hollow ion emission*, in "XFEL Technical Design Report", Chapter 6, p. 251-253, DESY 2006, http://xfel.desy.de/tdr/tdr

Rosmej, F.B. & Lee, R.W. (2007). *Hollow ion emission driven by pulsed x-ray radiation fields*, Europhysics Letters 77, 24001.

Rosmej, F.B. ; Lee, R.W. & Schneider, D.H.G (2007). *Fast x-ray emission switches driven by intense x-ray free electron laser radiation*, High Energy Density Physics 3, 218.

Rosmej, F.B.; Petitdemange, F. & Galtier, E. (2011). *Identification of Auger electron heating and inverse Auger effect in experiments irradiating solids with XUV Free Electron Laser Radiation at intensities larger than 10^{16} W/cm^2,* SPIE International Symposium on Optical Engineering and Applications "X-Ray Lasers and Coherent X-Ray Sources: Development and Applications (OP321)" (21–25/08/2011) San Diego, USA.

Rosmej, F.B & Lisitsa, V.S (2011): *"Non-equilibrium radiative properties in fluctuating plasmas"*, Plasma Physics Reports 37, 521.

Rosmej, F.B. (2012). *X-ray emission spectroscopy and diagnostics of non-equilibrium fusion and laser produced plasmas"*, in "Highly Charged Ions, editors Y. Zou and R. Hutton, Taylor and Francis 2012, ISBN 9781420079043.

SACLA 2011. http://xfel.riken.jp/eng

Seely, J.; Rosmej, F.B.; Shepherd, R.; Riley, D. & Lee, R.W. (2011). *Proposal to Perform the 1st High Energy Density Plasma Spectroscopic Pump/Probe Experiment*, accepted beam time proposal n° L332 at LCLS.

Sobelman, I.I.; Vainshtein, V.S.; Yukov & E.A. (1995). *Excitation of Atoms and Broadening of Spectral Lines*, Springer, Berlin, ISBN 3-540-58686-5.

Talin, B. ; Calisti, A. ; Godbert, L.; Stamm, R.; Lee, R. W. & Klein, L. (1995). *Frequency-fluctuation model for line-shape calculations in plasma spectroscopy*, Phys. Rev. A 51, 1918.

Tauschwitz, An. ; Maruhn, J.A. ; Riley, D. ; Shabbir Naz, G. ; Rosmej, F.B. ; Borneis, S. & Tauschwitz, A. 2007. *Quasi-isochoric ion beam heating using dynamic confinement in spherical geometry for X-ray scattering experiments in WDM regime"*, High Energy Density Physics 3, 371.

WIKI 2011. *http://en.wikipedia.org/wiki/List_of_Star_Trek_materials#Transparent_aluminum*

XFEL 2011. http://xfel.desy.de/

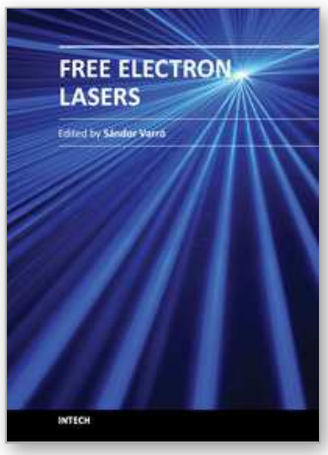

Free Electron Lasers

Edited by Dr. Sandor Varro

ISBN 978-953-51-0279-3
Hard cover, 250 pages
Publisher InTech
Published online 14, March, 2012
Published in print edition March, 2012

Free Electron Lasers consists of 10 chapters, which refer to fundamentals and design of various free electron laser systems, from the infrared to the xuv wavelength regimes. In addition to making a comparison with conventional lasers, a couple of special topics concerning near-field and cavity electrodynamics, compact and table-top arrangements and strong radiation induced exotic states of matter are analyzed as well. The control and diagnostics of such devices and radiation safety issues are also discussed. Free Electron Lasers provides a selection of research results on these special sources of radiation, concerning basic principles, applications and some interesting new ideas of current interest.

InTech Europe
University Campus STeP Ri
Slavka Krautzeka 83/A
51000 Rijeka, Croatia
Phone: +385 (51) 770 447
Fax: +385 (51) 686 166
www.intechopen.com

InTech China
Unit 405, Office Block, Hotel Equatorial Shanghai
No.65, Yan An Road (West), Shanghai, 200040, China
中国上海市延安西路65号上海国际贵都大饭店办公楼405单元
Phone: +86-21-62489820
Fax: +86-21-62489821

IntechOpen